Suppression of Coherence Matrix Bias for Phase Linking and Ambiguity Detection in MTInSAR

Hongyu Liang, *Graduate Student Member, IEEE*, Lei Zhang, *Senior Member, IEEE*, Xiaoli Ding, *Member, IEEE*, Zhong Lu, *Senior Member, IEEE*, Xin Li, Jun Hu, *Member, IEEE*, and Songbo Wu, *Graduate Student Member, IEEE*

***Abstract*— Phase decorrelation, as one of the main error sources, limits the capability of interferometric synthetic aperture radar (InSAR) for deformation mapping over areas with low coherence. Although several methods have been realized to reduce decorrelation noise, for example, by phase linking and spatial and temporal filters, their performances deteriorate when coherence estimation bias exists. We present an arc-based approach that allows reconstructing unwrapped interval phase time-series based on iterative weighted least squares (WLS) in temporal and spatial domains. The main features of the method are that phase optimization and unwrapping can be jointly conducted by spatial and temporal iterative WLS and coherence matrix bias has negligible effects on the estimation. In addition, the linear formation makes the implementation suitable with small subset of interferograms, providing an efficient solution for future big SAR data. We demonstrate the effectiveness of the proposed method using simulated and real data with different decorrelation mechanisms and compare our approach with the state-of-art phase reconstruction methods. Substantial improvement can be achieved in terms of reduced root-mean-square error (RMSE) in the simulation data and increased density of coherent measurements in the real data.**

***Index Terms*— Distributed scatterer (DS), interferometric synthetic aperture radar (InSAR), phase decorrelation, distributed scatterer weighted least squares (WLS).**

I. Introduction

INTERFEROMETRIC synthetic aperture radar (InSAR) nowadays represents a powerful tool for mapping ground deformation and topography with high spatial resolution over a wide coverage of the Earth's surface. In recent years, InSAR technique has been widely exploited in monitoring deformations caused by natural or anthropogenic activities, including volcanism [1], seismicity [2], landslides [3], and urban subsidence [4], [5]. It is no doubt that reliable interferometric measurements are the fundamental of accurate estimation of the geophysical parameters. The interferometric measurements between two SAR acquisitions comprise phase components related to parameters that can contribute to the change in the physical path between SAR satellite and ground target, and coherence that indicates the interferometric quality. Promoted by the next generation of SAR missions with better orbital control and shorter revisit cycle, the main challenges that currently limit InSAR capability lie in decorrelation noise reduction, phase unwrapping, and deformation isolation from confounding signals.

To tackle the decorrelation phenomenon, multitemporal InSAR (MTInSAR) technique featured by leveraging an extensive archive of SAR data stack has been developed. Persistent scatterer interferometry (PSI) [6]–[8], as a remarkable breakthrough in this field, was initially introduced to exploit the phase of stable point targets [i.e., persistent scatterers (PSs)] over the entire observation period. The basic strategy of PSI is to form single-master (SM) interferograms and estimate geophysical parameters (i.e., deformation rate and topographic error) from point-wise PSs that are less affected by temporal or spatial decorrelation. This method is effective in urban areas with abundant man-made structures, while it is compromised in rural areas due to the lack of PSs. To overcome this limitation, the PSI has been evolved to extract information from distributed scatterers (DSs) in addition to PSs. The DSs are referred to as the pixels whose coherence varies with spatiotemporal baselines. These pixels usually comprise a coherent sum of independent small scatterers with statistically homogeneous behavior. Based on the central limit theorem, the mechanism of DSs can be modeled by a complex circular Gaussian (CCG) radar return, of which the coherence values tend to decline with the rise in temporal and spatial separation between SAR acquisitions. Some work based on exploiting DSs has been conducted to minimize the decorrelation effect by generating the multiple-master (MM) interferograms from properly selected pairs, for example, short baseline subset (SBAS) method [5], [9], [10]. The selected interferograms suffer less decorrelation and are further spatially

Manuscript received December 27, 2019; revised April 30, 2020; accepted June 1, 2020. This work was supported in part by the National Natural Science Foundation of China under Grant 41774023, Grant 41304011, Grant 41874030, and Grant 41674010, and in part by the Research Grants Council of Hong Kong under Grant PolyU152232/17E and Grant PolyU152164/18E. *(Corresponding author: Lei Zhang.)*

Hongyu Liang, Lei Zhang, Xiaoli Ding, and Songbo Wu are with the Department of Land Surveying and Geo-Informatics, The Hong Kong Polytechnic University, Hong Kong (e-mail: allenhongyu.liang@connect.polyu.hk; lslzhang@polyu.edu.hk; xl.ding@polyu.edu.hk; sabriwu@outlook.com).

Zhong Lu is with the Roy M. Huffington Department of Earth Sciences, South Methodist University, Dallas, TX 75275 USA (e-mail: zhonglu@smu.edu).

Xin Li is with the Institute of Geographic Sciences and Natural Resources Research, Chinese Academy of Sciences, Beijing 100101, China (e-mail: vivianyoxi@gmail.com).

Jun Hu is with the School of Geosciences of and Info-Physics, Central South University, Changsha 410083, China (e-mail: csuhujun@csu.edu.cn).

Color versions of one or more of the figures in this article are available online at http://ieeexplore.ieee.org.

Digital Object Identifier 10.1109/TGRS.2020.3000991

multilooked (i.e., complex averaged) to enhance the signal-to-noise ratio (SNR) at the loss of spatial resolution. After spatial unwrapping, the SBAS method retrieves the deformation time series by least squares (LS) with the constraint of minimum norm [9], [10].

More recently, researches have been forwarded to extract the phase information of DSs by incorporating all interferometric combinations. The method typically assumes the radar return and the geophysical signal is consistent within a cluster of pixels. Jointly processing these pixels would improve the SNR and extend the spatial coverage of InSAR deformation maps [11]. The method usually commences identifying statistically homogeneous pixels (SHPs) by statistical similarity test based on amplitude information [11]–[13]. Then, phase linking (PL) (also called phase triangulation analysis (PTA) [11], [14]) procedure is adopted to estimate the wrapped SM phase time series based on the temporal consistency. Up to now, various PL algorithms have been realized, including maximum likelihood estimator (MLE) [11], [14], [15], eigenvalue decomposition (EVD) [16], [17], integer least squares (ILS) [18], and the integration of MLE and EVD [19]. Despite their diverse weighting strategies for the involved interferograms, their performances deteriorate in the presence of error in coherence estimation. Regarding the qualities of the estimated phases, although the PL methods reduce the decorrelation noise, the qualities after PL do not keep at the same level due to the diversity of the good-of-fit measurements [11], [18], [20]. The quality inconsistency of the estimated phases may propagate into the unwrapped phases, increasing uncertainties of the estimated geophysical parameters.

With respect to the aforementioned works, we present an arc-based approach that allows to reconstruct the unwrapped interval phase chain from the pixels with variable phase noise. The method uses two successive iterative weighted least squares (WLS) to first estimate the interval phase chain at arcs (i.e., point pairs) and then derive the unwrapped phase maps according to the estimated phase variance. The role of iterative WLS lies in twofold, that is, suppressing the effects of coherence estimation bias and phase ambiguities in the arc processing procedure and ensuring the estimation unbiased by considering the inconsistent phase quality in the spatial integration procedure. Improving the quality of unwrapped phase time series estimated from pixels with variable phase noise by iterative WLS is therefore the main feature of the method.

The rest of this article is organized as follows. Section II describes the detailed implementation of the LS-based phase estimation, including observation generation, temporal estimation, and spatial recovery. Sections III and IV are dedicated to the results of synthetic experiments and real data tests, followed by the conclusion in Section V.

II. Methodology

A. Observation Generation

The proposed method aims at estimating the unwrapped phase chain from all possible or selected interferograms. Let us start from a DS pixel in a stack of the SAR images.

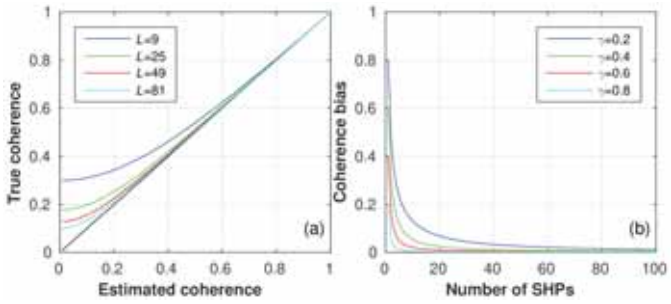

Fig. 1. Coherence estimation bias under different numbers of SHPs. (a) Relationship between the estimated coherence and true coherence under different numbers of SHPs. (b) Relationship between the number of SHPs and coherence bias under different estimated coherence values.

When two coregistered SAR images are available over a given area, after SHPs are identified by statistical similarity test between a specific pixel x and the neighboring pixels [11]–[13], the maximum likelihood estimation of sample complex coherence for the point x is expressed as

$$\mathbf{\Gamma}^{m,n} = \frac{\sum_{t=1}^{L} s^m(t) s^{n*}(t)}{\sqrt{\sum_{t=1}^{L} |s^m(t)|^2 \sum_{t=1}^{L} |s^n(t)|^2}} = \gamma^{m,n} e^{i\phi^{m,n}} \tag{1}$$

where m and n are the indexes of the master and slave SAR images, respectively. L is the number of identified SHPs, t is the index of identified SHPs; $s^m(t)$ and $s^n(t)$ represent the complex phase values of the SAR image pair; $*$ stands for complex conjugate; i is the imaginary unit; the coherence magnitude $\gamma^{m,n}$ defines the degree of coherence; and $\phi^{m,n}$ represents the spatially averaged interferometric phase. All amplitude values in (1) are normalized to compensate for the disturbance of amplitude among the SAR images [6], [16]. We remark that the estimation in (1) is biased, especially for a small number of SHPs and coherence magnitude close to zero (see Fig. 1) [12], [21]. Assuming there are N coregistered SAR images forming $N(N-1)/2$ interferometric combinations, the complex coherence matrix is extended as

$$\begin{aligned}\mathbf{\Gamma} &= \begin{bmatrix} 1 & \gamma^{1,2} e^{i\phi^{1,2}} & \cdots & \gamma^{1,N} e^{i\phi^{1,N}} \\ \gamma^{2,1} e^{i\phi^{m,n}} & 1 & \cdots & \gamma^{2,N} e^{i\phi^{2,N}} \\ \vdots & \vdots & \ddots & \vdots \\ \gamma^{N,1} e^{i\phi^{N,1}} & \gamma^{N,2} e^{i\phi^{N,2}} & \cdots & 1 \end{bmatrix} \\ &= \mathbf{\Upsilon} \circ \mathbf{\Phi} \end{aligned} \tag{2}$$

where $\mathbf{\Phi}$ is an $N \times N$ matrix that encapsulates the available interferometric phases, $\mathbf{\Upsilon}$ is an $N \times N$ matrix providing corresponding coherence values, and $\circ$ is the Hadamard product. The phase and coherence values serve as the basis of the following function and stochastic models for interval phase chain estimation, respectively. It should be noted that for DS, the $N(N-1)/2$ combinations in the coherence matrix are not redundant due to temporal inconsistency after spatial multilooking operation [18]. While for point-wise PS, the rank of the coherence matrix equals one, and $\phi^{m,n}$ represents the point-wise phase itself. In the following, we will jointly process DSs and PSs as coherent points based on their phase and coherence values.

B. Unwrapped Phase Chain Estimation at Arcs

We first take the phase differences at arcs as the observations for phase chain estimation. The advantage of arc-based observations is that the probability of phase ambiguity after differencing between the neighboring points will be largely reduced, benefiting a linear formation of the follow-on phase estimation [22]. The differencing network can be constructed by local Delaunay triangulation [23] or k-nearest neighbor algorithm [24]. The high density of network allows a redundant set of differential measurements (not only between nearest ones), which aids a reliable spatial integration [25].

For a specific arc, we assume that $\boldsymbol{\Delta\phi} = (\Delta\phi^{1,2}, \Delta\phi^{1,3}, \ldots, \Delta\phi^{m,n}, \ldots, \Delta\phi^{N-1,N})^{\mathrm{T}}$ is the vector of wrapped phase difference in $N(N-1)/2$ interferometric pairs, and $\boldsymbol{\Delta\varphi} = (\Delta\varphi^{1}, \Delta\varphi^{2}, \ldots, \Delta\varphi^{m}, \ldots, \Delta\varphi^{N-1})^{\mathrm{T}}$ is the vector of unknown phase difference for $N-1$ sequential intervals. The function model for the phase chain at arc is expressed as

$$\boldsymbol{B\Delta\varphi} = \boldsymbol{\Delta\phi} \tag{3}$$

with

$$\begin{aligned} \boldsymbol{\Delta\widehat{\varphi}} &= (\boldsymbol{B}^{\mathrm{T}}\bar{P}\boldsymbol{B})^{-1}\boldsymbol{B}^{\mathrm{T}}\bar{P}\boldsymbol{\Delta\phi} \\ \boldsymbol{V} &= \boldsymbol{\Delta\phi} - \boldsymbol{B\Delta\widehat{\varphi}} \\ v^{m,n} &= \Delta\phi^{m,n} - b^{m,n}\boldsymbol{\Delta\widehat{\varphi}} \end{aligned} \tag{4}$$

where $\boldsymbol{B}$ is the design matrix that connects interferometric pairs and sequential intervals through the combination of 0 and 1. $\boldsymbol{\Delta\widehat{\varphi}}$ represents the estimate of $\boldsymbol{\Delta\varphi}$. $\boldsymbol{V}$ is an $(N(N-1)/2)\times 1$ residual vector and $v^{m,n}$ represents one element of $\boldsymbol{V}$, $b^{m,n}$ indicates one element of $\boldsymbol{B}$, and $\bar{P}$ is called the equivalent weight matrix, which adjusts the influence of observations to fit the actual accuracy of the corresponding observations [26]. We remark that in (3), the phase difference observations with ambiguities will be detected as outliers and suppressed by iterative WLS operation.

C. Iteratively Weight Updating

The purpose of iteratively weight updating is to provide robust estimates that are unaffected by outliers or skewed residual distributions. This is performed by making use of information from all observations while assigning less or even zero weight to those observations with large residuals [27]. The unusual observations in this study are attributed to not only the phase ambiguities but also the phase error due to coherence estimation bias and signal inconsistency in the averaged area [18]. To mitigate these effects, the equivalent weight matrix $\overline{\boldsymbol{P}}$ is used which can be expressed as

$$\overline{\boldsymbol{P}} = \boldsymbol{P} \circ \boldsymbol{G} \tag{5}$$

where $\boldsymbol{P}$ is the initial weight matrix which has a diagonal form and can be determined by the coherence matrix and multilooking factor (see the Appendix). $\boldsymbol{G}$ is also a diagonal matrix $\mathrm{diag}(g^{1,1}, g^{2,2}, \ldots, g^{m,n}, \ldots, g^{N,N})$, where the diagonal element represents the down-weighting factor for each observation and the expression varies depending on different down-weight functions. In this study, we choose the commonly used biweight function as (see Fig. 2)

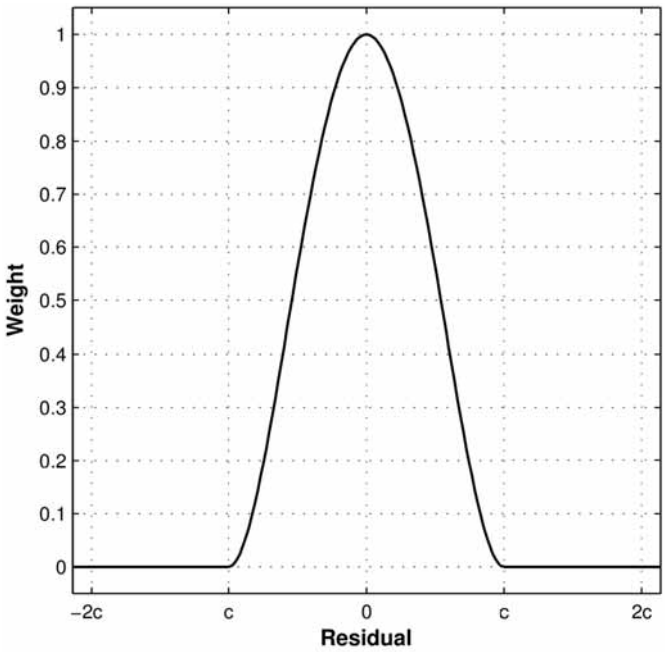

Fig. 2. Curve of the biweight function, where c is a tuning constant depending on the distribution of samples.

$$g^{m,m} = \begin{cases} \left[1 - \left(u^{m,m}/c\right)^2\right]^2, & |u^{m,m}| \le c \\ 0, & |u^{m,m}| > c \end{cases} \tag{6}$$

with

$$u^{m,m} = \frac{v^{m,m}}{s\sqrt{1-h^{m,m}}} \tag{7}$$

where $u^{m,m}$ represents the normalized residual, $h^{m,m}$ is the hat value giving the leverage of observations [28] which is derived from the diagonal element of $\boldsymbol{B}(\boldsymbol{B}^{\mathrm{T}}\boldsymbol{B})^{-1}\boldsymbol{B}^{\mathrm{T}}$, s is the median absolute deviation (MAD), and c is a tuning constant which is usually set as 4.685, producing 95% efficiency at normal distribution [29].

As a summary, the solution of (4) can be derived in the following three steps.

1) Use the initial weight matrix $\boldsymbol{P}$ to replace $\overline{\boldsymbol{P}}$ and derive the initial solution by (4).
2) Based on the LS residuals in (4), calculate the down-weight factor matrix by (6) and (7), and perform WLS estimation again with the updated weight matrix by (5).
3) Repeat step 2) until $\left|\boldsymbol{\Delta\widehat{\varphi}}^{b+1} - \boldsymbol{\Delta\widehat{\varphi}}^{b}\right| < \eta$; η is a predefined threshold.

D. Low-Quality Arc Rejection

It should be noted that the iterative weight updating scheme has an upper limit (up to 50%) to resist unusual observations [27], and therefore, the arc measurements that are corrupted by overwhelming outliers or decorrelation noise should be discarded. The low-quality arcs can be detected by equivalent

temporal coherence (ETC)

$$\gamma_{\overline{\boldsymbol{P}}} = \frac{\left|\sum \overline{\boldsymbol{P}} \cdot e^{i(\boldsymbol{\Delta\phi} - \boldsymbol{B}\boldsymbol{\Delta}\widehat{\boldsymbol{\varphi}})}\right|}{\mathrm{tr}(\overline{\boldsymbol{P}})} \tag{8}$$

where $\mathrm{tr}(\cdot)$ is the operator for calculating the trace of a matrix. The merit of using the weight matrix $\overline{\boldsymbol{P}}$ in (8) is that it suffers less effect from outliers in observations by assigning zero weight on them. By setting threshold $\gamma_{\overline{\boldsymbol{P}}}^{\mathrm{thre}}$, the suspected arcs with $\gamma_{\overline{\boldsymbol{P}}} \leq \gamma_{\overline{\boldsymbol{P}}}^{\mathrm{thre}}$ are discarded. Generally, the value of $\gamma_{\overline{\boldsymbol{P}}}^{\mathrm{thre}}$ can be set as 0.7–0.9 [6], [18], and it will be further discussed in Section III-A. Moreover, the observations with undetected phase ambiguities are further removed by triplet closure in space, where the closure threshold can be set as 1 rad [22], [30].

E. Spatial Integration

After calculating the unwrapped interval phase chain at arcs and removing the low-quality arcs, the isolated points should be detected and deleted to avoid local errors of spatial integration [31], [32]. As aforementioned, the reconstructed phases at pixels with different scattering mechanisms have different noise levels. The inconsistency of phase quality at a given arc can be addressed by the *posteriori* covariance matrix [26]

$$\boldsymbol{D}_{\boldsymbol{\Delta}\widehat{\boldsymbol{\varphi}}} = \left(\boldsymbol{B}^{\mathrm{T}}\overline{\boldsymbol{P}}\boldsymbol{B}\right)^{-1}\widehat{\sigma}_0^2 \tag{9}$$

with

$$\widehat{\sigma}_0^2 = \frac{\boldsymbol{V}^{\mathrm{T}}\overline{\boldsymbol{P}}\boldsymbol{V}}{M' - (N-1)} \tag{10}$$

where $\boldsymbol{D}_{\boldsymbol{\Delta}\widehat{\boldsymbol{\varphi}}}$ is the *posteriori* covariance matrix of the estimated $\boldsymbol{\Delta}\widehat{\boldsymbol{\varphi}}$, and M' is the number of effective observations after outlier removal based on the biweight function. The unwrapped interval phase vector at each pixel then can be derived by performing WLS on the estimated phase chain with the *posteriori* variances of arcs. Assuming the remained network includes E points and F arcs, the formulation between the phase $\boldsymbol{\Phi}^m$ at points and the phase difference at arcs for each interval epoch is expressed as

$$\boldsymbol{A}\boldsymbol{\delta\varphi}^m = \boldsymbol{\Delta\varphi}^m \tag{11}$$

with

$$\boldsymbol{\delta\varphi}^m = \left(\boldsymbol{A}^{\mathrm{T}}\boldsymbol{W}^m\boldsymbol{A}\right)^{-1}\boldsymbol{A}^{\mathrm{T}}\boldsymbol{W}^m\boldsymbol{\Delta\varphi}^m \tag{12}$$

where $\boldsymbol{A}$ is the network matrix linking points and arcs, in which the reference point has been removed. The network matrix has the form

$$\boldsymbol{A} = \begin{bmatrix} 1 & 0 & -1 & \cdots & 0 \\ 0 & 1 & \cdots & -1 & 0 \\ \vdots & \vdots & \vdots & \vdots & \vdots \\ 0 & 0 & 1 & 0 & -1 \end{bmatrix} \tag{13}$$

where 1 represents the starting point and -1 corresponds to the ending point along each arc. $\boldsymbol{W}$ is an $F \times F$ diagonal matrix, of which the element is determined by

$$\boldsymbol{W}^m = \mathrm{diag}\left(\frac{1}{d_{\Delta\widehat{\varphi}_1^m}+\varepsilon}, \frac{1}{d_{\Delta\widehat{\varphi}_2^m}+\varepsilon}, \ldots, \frac{1}{d_{\Delta\widehat{\varphi}_i^m}+\varepsilon}, \ldots, \frac{1}{d_{\Delta\widehat{\varphi}_E^m}+\varepsilon}\right) \tag{14}$$

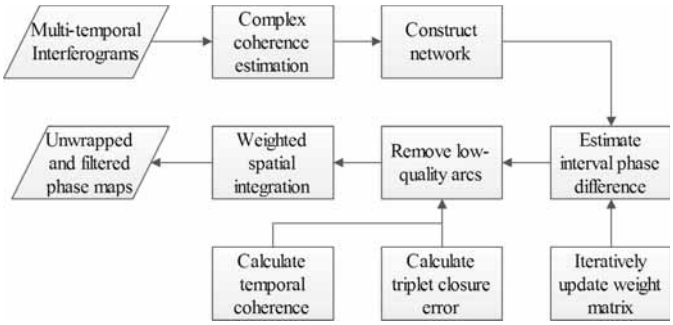

Fig. 3. Flowchart of the proposed method.

where ε is a small positive constant to avoid the denominator being zero. It should be noted that as the interferometric phase is a relative measurement, the scatter noise of the reference point will manifest itself in other points through network differencing and integration. To mitigate this error, before spatial integration, we select a high-coherence point (e.g., PS) as the reference. Then, spatial integration is implemented for each interval epoch with respect to the reference point. Because the reference point may not be stable, after spatial integration all points can be calibrated with respect to a new reference point which is postulated as stable behavior in time series.

F. Algorithm Flow

The algorithm flowchart is shown in Fig. 3, and the whole procedure is described as follows.

1) For each pixel, calculate the complex coherence matrix based on the identified SHPs.
2) Construct spatial network and build function model between MM interferograms and phase differences in sequential intervals at arcs.
3) At each arc, conduct WLS estimation to obtain the interval phase differences by iteratively updating weight matrix.
4) Calculate the temporal coherence and triplet closure error at arcs and remove the arcs with low temporal coherence or large triplet closure error.
5) Conduct weighted spatial integration based on unwrapped phase difference and the associated *posteriori* phase variance in each interval epoch.

III. Synthetic Data Tests

To validate the proposed method and assess its performance, a set of experiments are conducted based on synthetic data sets in this section. We first test the robustness of the proposed estimation on a single arc and then perform the overall evaluation of phase reconstruction on simulated interferograms.

A. Test on a Single Arc

Observations at a single arc are generated with different levels of decorrelation noise and outlier (i.e., phase ambiguities) contamination. The baselines of interferograms generated from 23 SAR acquisitions are retrieved from the real Sentinel-1 data

TABLE I
SENTINEL-1 DATA BASELINE INFORMATION

No.	Date	Perpendicular baseline (m)	Temporal baseline (day)
1	20160913	0	0
2	20160925	-60	12
3	20161007	-26	24
4	20161019	54	36
5	20161031	36	48
6	20161112	35	60
7	20161124	-5	72
8	20161206	-43	84
9	20161218	-29	96
10	20161230	-8	108
11	20170111	54	120
12	20170123	36	132
13	20170204	12	144
14	20170216	36	156
15	20170228	65	168
16	20170312	16	180
17	20170324	43	192
18	20170405	-18	204
19	20170417	-77	216
20	20170429	24	228
21	20170511	-36	240
22	20170523	31	252
23	20170604	-35	264

set (Frame 68, Track 11) (Table I) over Guangdong, China. We use C-band Sentinel-1 data set in simulation because the short wavelength and revisit cycle render the data set sensitive to temporal decorrelation. For simplicity, we assume a deformation signal with a rate of 5 mm/year at the arc. Considering that the proposed method aims to recover the unwrapped interval phases instead of the deformation signal, such an assumption does not lose generality. The decorrelation noise is generated from a random vector of complex values that follow zero-mean CCG distribution. In this study, two decorrelation models are introduced, that is, exponential decay and seasonal decay. The former one is expressed as

$$\gamma^{m,n} = \gamma_0 e^{\frac{-B_T^{m,n}}{\tau_0}} \tag{15}$$

where $B_T^{m,n}$ is the temporal baseline between SAR acquisition m and n, γ_0 represents the initial coherence value, and τ_0 is the time constant of the exponential decay rate. The second decorrelation model has a more complex expression as [33]

$$\gamma^{m,n} = \gamma_0 e^{\frac{-B_T^{m,n}}{\tau_0}} \cdot e^{\frac{T\cdot\left[\cos\left(\frac{2\pi}{T}(B_T^m+B_T^{m,n}-t_0)\right)-\cos\left(\frac{2\pi}{T}(B_T^m-t_0)\right)\right]}{2\pi\tau_1}} \tag{16}$$

where B_T^m represents the date of maser observation, τ_1 is the time constant of the seasonal decay rate, and T and t_0 are the period and the initial time of seasonal variation, respectively. The above two models manifest as two common decorrelation behaviors in real cases [11], [18]. To investigate the robustness of the proposed method in different circumstances, for each decorrelation model, we construct four scenarios by varying the model parameters. Table II lists the used model parameters for each decorrelation scenario. Based on the simulated decorrelation noise, the coherence matrices are computed from 23 acquisitions with 400 SHP samples using (15) and (16) (Fig. 4).

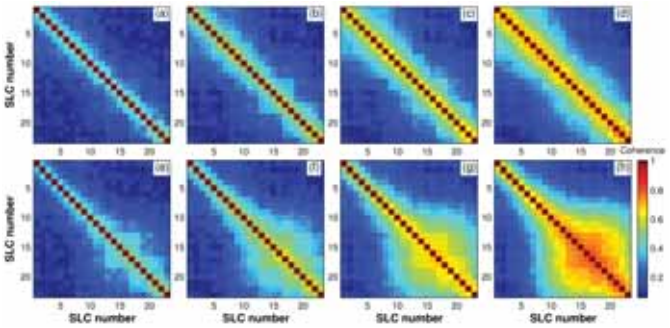

Fig. 4. Estimated coherence matrices of the synthetic data with exponential and seasonal decorrelation decay models. (a)–(d) Exponential decay. (e)–(h) Seasonal decay. The decorrelation model parameters: case 1 is used in (a) and (e), case 2 in (b) and (f), case 3 in (c) and (g), and case 4 in (d) and (h).

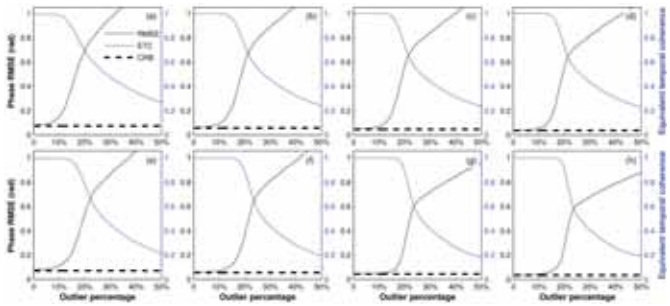

Fig. 5. RMSE of phase estimation by the proposed method under different decorrelation scenarios. (a)–(d) Exponential decay. (e)–(h) Seasonal decay. The decorrelation model parameters: case 1 is used in (a) and (e), case 2 in (b) and (f), case 3 in (c) and (g), and case 4 in (d) and (h).

To validate the robustness of estimation to detect outliers (i.e., phase ambiguity), we use all interferometric combinations (i.e., 253 interferometric combinations) and randomly add phase ambiguities into the original observations. The percentage of contaminated observations ranges from 1% to 50% of the total interferograms. For each number of observations that suffer phase ambiguities, we repeat 3000 times without replacement and calculate the root-mean-square error (RMSE) between the simulated and the estimated phase difference in sequential intervals. Fig. 5 presents the estimation performance of the proposed method under different decorrelation scenarios. It can be seen that when the outlier percentage is small, the estimation precision approximately approaches to the lowest achievable standard deviation, which is calculated by the Cramér–Rao bound (CRB) [34] based on the theoretical coherence values. Closer inspection of Fig. 5 indicates that with the decrease in the decorrelation noise level, the breakpoint (i.e., the largest percentage of the outlier that the robust estimation can tolerate without producing arbitrary results) increases and reaches up to about 20% of the total observations. This means that even a portion of the observations suffers phase ambiguities, and the method based on iterative weight update can still provide stable results and the tolerance percentage depends on the decorrelation noise level.

Meanwhile, during each estimation, we calculate the ETC as an indicator of the *posteriori* quality of the arc. Comparing the estimated RMSE and ETC reveals that once the estimation is

TABLE II
DECORRELATION MODEL PARAMETERS FOR DIFFERENT SCENARIOS

Case number	Exponential decay	Seasonal decay
Case 1	$\gamma_0 = 0.8, \tau_0 = 80$	$\gamma_0 = 0.8, \tau_0 = 80, \tau_1 = 90, t_0 = 280$
Case 2	$\gamma_0 = 0.7, \tau_0 = 70$	$\gamma_0 = 0.7, \tau_0 = 70, \tau_1 = 90, t_0 = 280$
Case 3	$\gamma_0 = 0.6, \tau_0 = 60$	$\gamma_0 = 0.6, \tau_0 = 60, \tau_1 = 90, t_0 = 280$
Case 4	$\gamma_0 = 0.5, \tau_0 = 50$	$\gamma_0 = 0.5, \tau_0 = 50, \tau_1 = 90, t_0 = 280$

corrupted by overwhelming phase ambiguities and/or decorrelation noises, the suspect arcs can be detected by the decline in ETC measures. The detection of outliers facilitates the discard of the corrupted arc measurements before subsequent spatial integration. It is also observed that when ETC is less than 0.85, the estimated phase differences significantly deviate from the simulated values. Therefore, to be a conservative treatment, the threshold of ETC is set as 0.85 or above.

B. Test on Interferograms

The effectiveness of the proposed method is tested and compared with the state-of-the-art phase estimation methods based on synthetic interferograms. In the test, we generate two interferogram stacks using the Sentinel-1 baseline that is shown in Table I. For simplicity, the components of each interferogram include deformation, atmospheric delays, and decorrelation noise. The deformation field is simulated using peak function in MATLAB with a linear rate ranging from -30 to 30 mm/year. The atmospheric delays are simulated using a fractal surface with the fractal dimension being 2.2. To investigate the phase estimation in different decorrelation models, one interferogram stack only contains exponential decay decorrelation noise, while the other one contains seasonal decay decorrelation noise. Within each stack, to be close to the real environment, we consider the mixture of multiple decorrelation levels [35], [36]. Table III lists the occupation percentages for different noise scenarios, of which the decorrelation parameters are listed in Table II [15], [19]. Fig. 6 shows the average coherence maps from the two interferogram stacks. Figs. 7(a) and (b) and 8(a) and (b) display the simulated SM interferograms without and with decorrelation noise, respectively.

We apply the proposed method to reconstruct the interval phase chains from all interferometric combinations. Before implementation, the coherence values and the multilooked phases are calculated by spatially averaging over 9×9 windows. Figs. 7(c) and 8(c) show the SM interferograms after spatial multilooking. After performing the proposed estimation, we convert the derived unwrapped interval phases into SM interferograms with respect to the first image [Figs. 7(d) and 8(d)]. The residuals between the reconstructed and the simulated phase signals are shown in Figs. 7(e) and 8(e). The accumulative phase residuals between the reconstructed and the simulated phases have a mean value of 0.07 rad and a standard deviation of 0.35 rad for exponential decay scenario, and a mean value of -0.08 rad and a standard deviation of 0.38 rad for seasonal decay scenario. As seen from Figs. 7 and 8, for both decorrelation decay models, the proposed method provides an unbiased estimate. The decorrelated noise

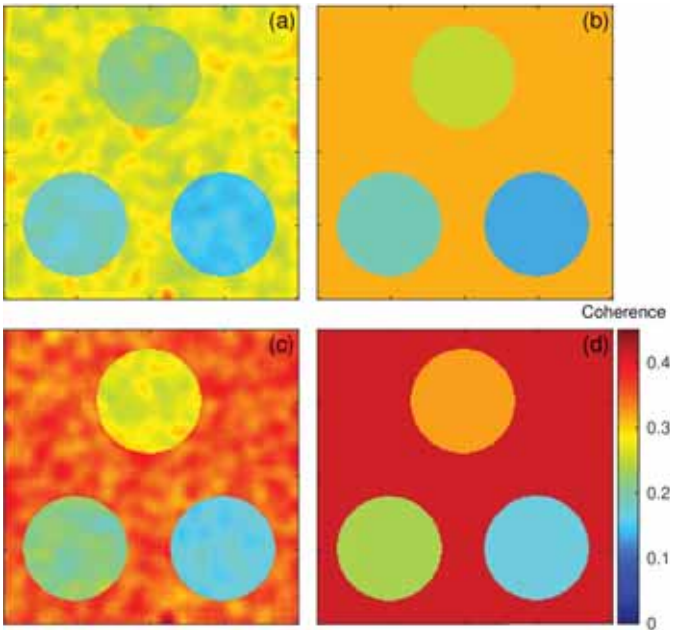

Fig. 6. Average coherence maps in the estimated and theoretical values. (a) and (c) Coherence estimated by 9×9 windows under exponential and seasonal decay, respectively. (b) and (d) Their theoretical coherence values.

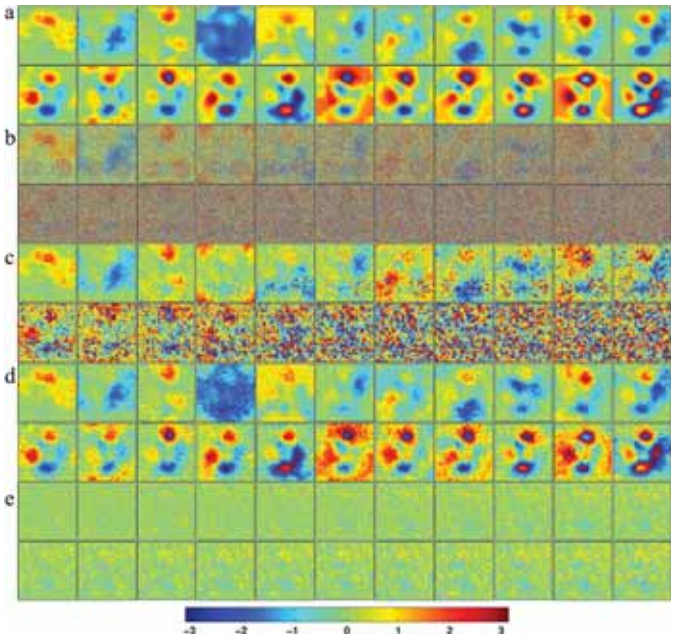

Fig. 7. Comparison of the original and reconstructed SM interferograms in the exponential decay scenario. All SM interferograms use the first image as the master image. (a) Original SM interferograms without decorrelation noise. (b) SM interferograms with decorrelation noise. (c) Multilooked SM interferograms. (d) Reconstructed SM interferograms by the proposed method. (e) Phase difference between the reconstructed and the original phase.

is effectively filtered out, yielding reconstructed phases with acceptable precision.

To further quantitively assess the performance of the proposed method, we compare the method with the combination of the state-of-the-art phase estimation (i.e., MLE [11], [14] and EVD [16], [17]) and phase unwrapping methods (i.e.,

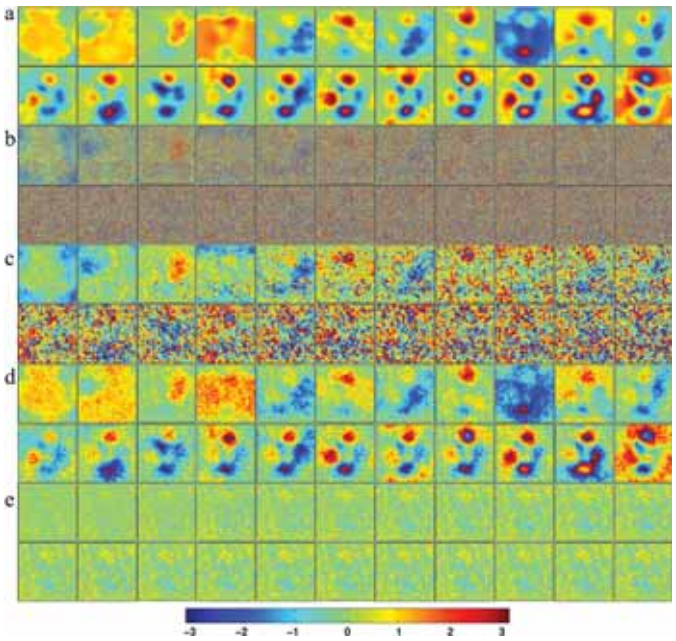

Fig. 8. Comparison of the original and reconstructed SM interferograms in the seasonal decay scenario. All SM interferograms use the first image as the master image. (a) Original SM interferograms without decorrelation noise. (b) SM interferograms with decorrelation noise. (c) Multilooked SM interferograms. (d) Reconstructed SM interferograms by the proposed method. (e) Phase difference between the reconstructed and the original phase.

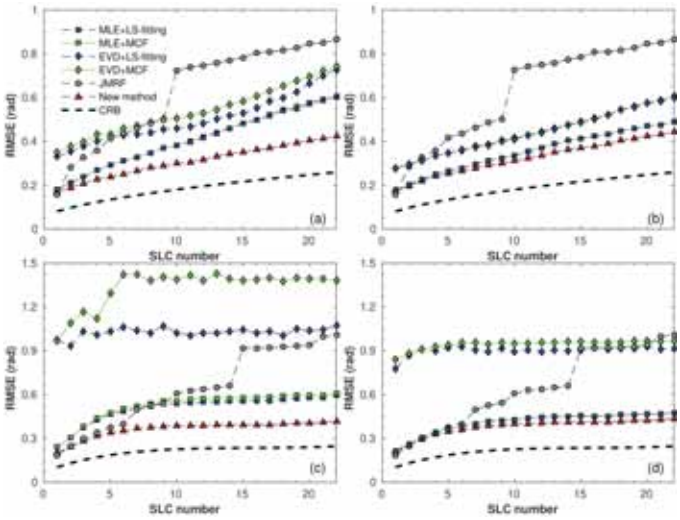

Fig. 9. Performance assessment of different phase estimation methods using simulated interferograms. (a) Exponential decay situation with estimated coherence values. (b) Exponential decay situation with theoretical coherence values. (c) Seasonal decay situation with the estimated coherence values. (d) Seasonal decay situation with the theoretical coherence values. For comparison, the CRB values of point cluster 1, which are calculated based on the parameters of case 1 of exponential and seasonal decays, are also plotted in four cases.

minimum cost flow (MCF) [37] and LS-fitting [38]) and a joint filtering and unwrapping method based on Markov random fields (JMRF) [39], [40]. As reflected in [15], [18], and [19], the error in the coherence matrix could significantly degrade the performance of phase estimation. To assess this impact, we divide the estimation processes into two groups. In the first group, the coherence matrices are estimated using the window size of 9×9. In the second group, the coherence matrices are assigned with the theoretical values. Fig. 6 shows the comparison of the estimated and theoretical average coherence maps. It is clear that the window size of coherence estimation has an obvious effect on coherence estimation. The 9×9 window size can lead to the maximum coherence bias of about 0.1 in a single interferogram. After the noisy phases are reconstructed and unwrapped by the above methods, the RMSE between the recovered and the simulated phase is calculated. The CRB for the decorrelation scenario of case 1 in Table II is calculated as well. Fig. 9 presents the comparison results of different estimation methods. We notice that no matter for MCF or LS-fitting phase unwrapping methods, when the coherence matrices change from the estimated to the theoretical values, the results of MLE and EVD vary significantly, manifesting their strong sensitivities to the quality of coherence estimation. Because both MLE and EVD reconstruct SM phase time series through the inversion and the decomposition of the coherence matrix, a small numerical bias of coherence will be amplified during matrix conversion, degrading the estimation precision. For the JMRF algorithm that only works for a single interferogram, although it shows low sensitivity to coherence bias, the phase recovery performance is limited by ignoring the relationship among interferograms. In the case of the proposed method, least difference is observed between the results of using the estimated and theoretical coherence values. This is because the proposed method iteratively adjusts the weight matrix according to the *posteriori* residuals, promoting the balance between the estimated coherence and the *posteriori* residuals.

From Fig. 9, we also notice that when using the theoretical coherence values, the proposed method still performs better than the MLE +MCF and MLE+LS-fitting. Although the MLE method has the best efficiency provided with a known accurate coherence matrix, the optimization is restricted within areas having a single decorrelation mechanism. Obviously, in practice, it is rare that areas only have one decorrelation mechanism. The MCF and LS-fitting algorithm ignore the variation in noise level due to the mixture of multiple decorrelation mechanisms, degrading the unwrapping performance. It should be noted that the CRB in four scenarios is always below other estimation results. This is attributed to the mixture of four decorrelation mechanisms (i.e., cases 1, 2, 3, and 4) which degrade the overall estimation precision.

In terms of computational efficiency, it is difficult to compare different methods, as the run-time strongly depends on the implementation of different estimators. Excluding coherence estimation and phase multilooking, a rough comparison is presented in Table III based on a desktop PC with an Intel

TABLE III
OCCUPATION PERCENTAGES FOR DIFFERENT NOISE SCENARIOS

Decorrelation model	Case 1	Case 2	Case 3	Case 4
Exponential decay	70%	10%	10%	10%
Seasonal decay	70%	10%	10%	10%

TABLE IV

COMPARISON OF THE COMPUTATION TIME (IN seconds) OF DIFFERENT PHASE ESTIMATION METHODS

Method	Exponential decay scenario (s)	Seasonal decay scenario (s)
MLE+LS-fitting	55.5	56.3
MLE+MCF	109.2	147.7
EVD+LS-fitting	13.6	14.1
EVD+MCF	186.5	1181.2
JMRF	7513.1	7549.2
Proposed method	350.9	360.3

TABLE V

ALOS/PALSAR DATA BASELINE INFORMATION

No.	Date	Perpendicular baseline (m)	Temporal baseline (day)
1	20070128	0	0
2	20070915	1564	230
3	20071216	2218	322
4	20080131	2654	368
5	20080502	3384	460
6	20080617	196	506
7	20080917	-1204	598
8	20081218	-867	690
9	20090202	-333	736
10	20090620	465	874
11	20090805	-21	920
12	20090920	578	966
13	20091221	1224	1058
14	20100205	1745	1104
15	20100508	2193	1196
16	20100623	2102	1242

i7 CPU and 64-GB memory. As can be seen from Table IV, high computation time might be the main drawback of the proposed method. Because the dense network and outlier detector slow the computation efficiency. However, considering the unwrapped phase product is obtained and further phase unwrapping procedure is no longer needed, the high computation time is acceptable.

IV. REAL DATA TEST

A stack of 16 ALOS/PALSAR images over Zhouqu, China (Table V) (Fig. 10), is chosen for assessment of the proposed method. Located at the eastern edge of Qinghai–Tibet Plateau, Zhouqu is characterized by steep terrain and alpine valleys, which render this area vulnerable to landslide-related geohazards. On August 8, 2010, a large landslide in Zhouqu caused widespread destruction and nearly 1800 casualties [41]. The deformation phenomenon in this area has been analyzed by conventional PSInSAR [3], [42], and it is suitable to validate the effectiveness of the method in low-coherence environment. Fig. 11 presents the spatiotemporal distribution of the radar images. As apparent, some interferograms have long spatial and temporal baselines, implying severe spatial and temporal decorrelation. Fig. 12(a) shows four examples of single-looking SM interferograms with the first SAR acquisition being the master image.

We apply the proposed method to reconstruct SM interferograms from all interferometric combinations [Fig. 11(a)]. The coherence value and multilooked phase for each pixel

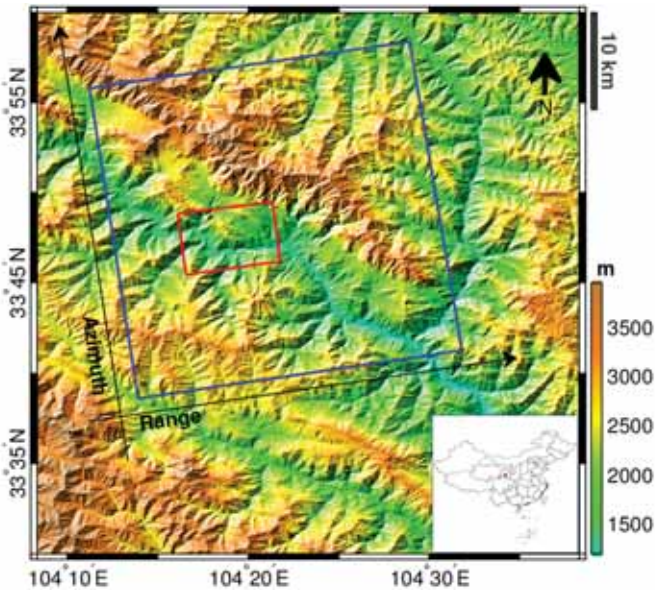

Fig. 10. Shaded relief map over Zhouqu, China. The blue solid box outlines the coverage of the ascending ALOS/PALSAR images (track 660) used in this study. The red solid outlines the study area. The inset map shows the location of the study area in China.

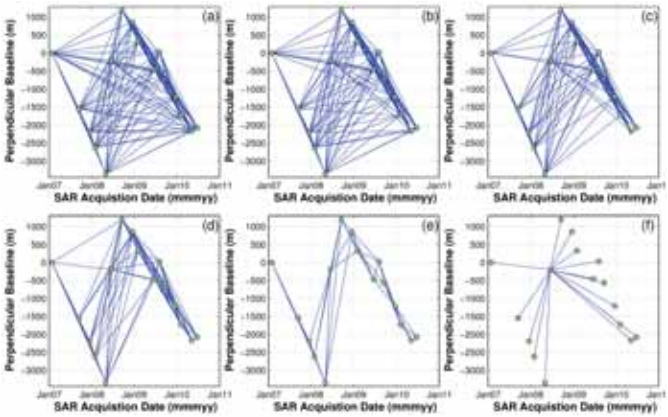

Fig. 11. Baseline configuration used in real data tests. (a) All interferometric combinations. (b)–(e) Interferometric combinations with short temporal baseline. Each SAR image has 12 lag interferograms in (b), 9 lag interferograms in (c), 6 lag interferograms in (d), and 3 lag interferograms in (e). (f) SM interferometric combinations using the sixth SAR acquisition as the master image.

are calculated by adaptively averaging SHPs detected by the Kolmogorov–Smirnov test [11]. To improve the spatial stationarity within multilooking windows, we use AW3D30m digital surface model (DSM) [43] to remove the topographic phase contribution before coherence estimation. Based on the coherence map, we initially select 1 220 475 coherent points (including PSs and DSs) for network construction and interval phase chain estimation. The arcs with low *posteriori* ETC are discarded, resulting in 1 192 913 points kept for spatial integration. The reconstructed interferograms can be visually inspected from Figs. 12 and 13. Comparing Fig. 12(b) and (c) shows that the decorrelation noise is effectively filtered by the proposed method, revealing the importance of tem-

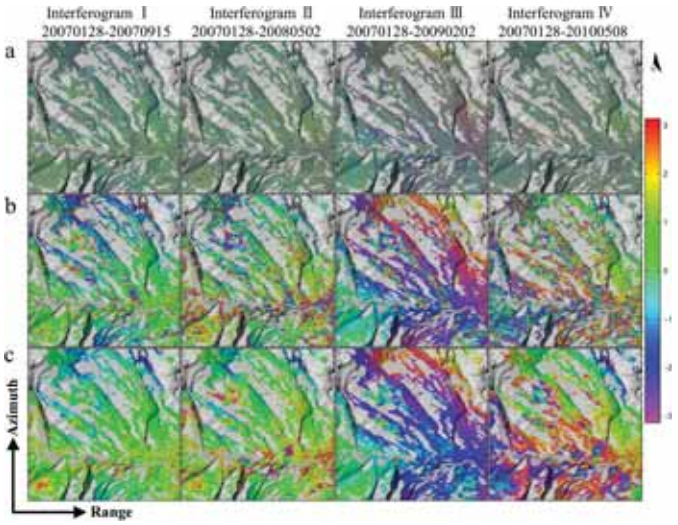

Fig. 12. Comparison of the original and reconstructed SM interferograms for ALOS/PALSAR images over Zhouqu, China. All SM interferograms use the first image as the master image. (a) Represents SM interferograms before multilooking. (b) Represents SM interferograms after multilooking. (c) Represents the reconstructed SM interferograms by the proposed method in wrapped form. Interferogram I has a perpendicular baseline of 1564 m and a temporal baseline of 230 days. Interferogram II has a perpendicular baseline of 3384 and a temporal baseline of 460 days. Interferogram III has a perpendicular baseline of −333 m and a temporal baseline of 736 days. Interferogram IV has a perpendicular baseline of 2193 m and a temporal baseline of 1196 days.

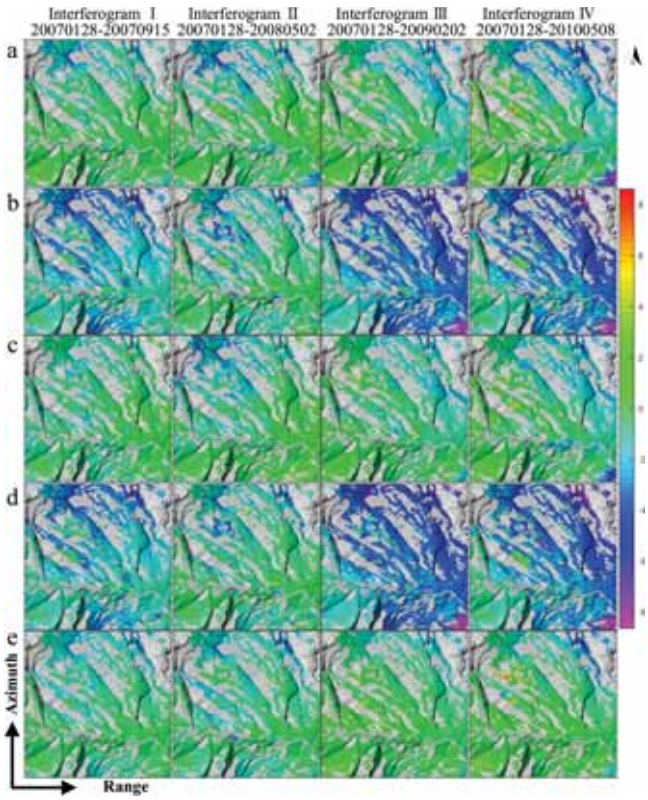

Fig. 13. Comparison of the recovered unwrapped SM interferograms between the proposed method and the combination of the existing phase estimation and phase unwrapping methods. (a) Represents the recovered unwrapped SM interferograms by MLE and LS-fitting. (b) Represents the recovered unwrapped SM interferograms by MLE and MCF. (c) Represents the recovered unwrapped SM interferograms by EVD and LS-fitting. (d) Represents the recovered unwrapped SM interferograms by EVD and MCF. (e) Represents the recovered unwrapped SM interferograms by the proposed method.

poral filtering other than spatial multilooking. Fig. 13 shows the comparison of the recovered unwrapped interferograms between the proposed method and the combination of the existing phase estimation (i.e., MLE and EVD) and phase unwrapping (i.e., MCF and LS-fitting) methods. It can be noticed that the phase jumps are identified from the unwrapped results of both MCF and LS-fitting on the lower right of the SAR image. In terms of phase estimation, the proposed method shows the best performance in reserving the sliding deformation signal in the middle of the SAR image.

The performance of using interferogram subsets is evaluated as well. Fig. 11(b)–(e) depicts the baseline configurations for four subsets of combinations. By setting the result of using all interferometric combinations [Fig. 11(a)] as a benchmark for this analysis, we calculate the accumulative phase differences between using the subsets and all combinations. Fig. 14 shows the histograms of the accumulative discrepancies for different subsets used. We can notice that the estimations using four kinds of subsets [i.e., Fig. 11(b)–(e)] provide unbiased estimation with respect to that using all combinations. However, the discrepancies are governed by the total number of combinations. As depicted, when the number of lag interferograms for each SAR image reduces from 12 to 3, the phase discrepancies rapidly increase, indicating the performance of estimation declines with the number of interferometric combinations. Therefore, to preserve high estimation precision, a large number of interferometric combinations are necessary for practical implementation.

To further validate the performance of phase estimation, we retrieve the deformation field based on the SM

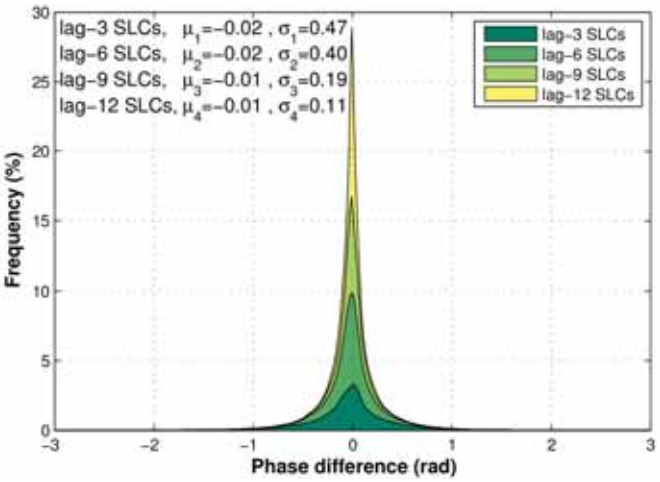

Fig. 14. Histograms of the accumulative discrepancies between using subsets and all combinations by the proposed method.

interferograms that are constructed from the estimated unwrapped interval phases. As the interferograms have no phase ambiguity, topographic residuals and atmospheric delays can be efficiently separated by [31] and [44]. For comparison, we apply the standard PSI to process the original

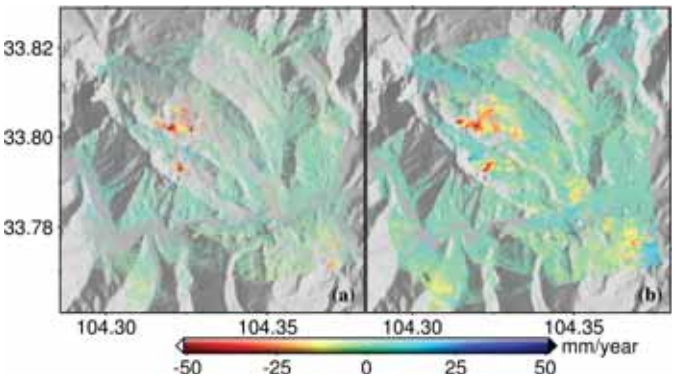

Fig. 15. Comparison of the deformation rate maps for the study area using (a) StaMPS PSI processing and (b) the proposed method.

single-looking interferograms [see the baseline configuration in Fig. 11(f)] using StaMPS software [45]. Fig. 15 presents the deformation rate maps from StaMPS and the proposed method. It can be seen that the deformation fields from the two methods are in good agreement, where the slopes facing the northeast show downslope movement with a line-of-sight velocity up to 5 cm/year. The deformation results are also consistent with previous studies about the Zhouqu landslides [3], [42]. It is also visible that through the phase estimation procedure, the spatial density of the coherent points significantly increases. The notable improvement in point density facilitates identifying sliding regions and further interpretation of landslide behavior.

V. Conclusion

In this article, we have proposed an arc-based method to reduce the decorrelation noise and reconstruct unwrapped interval phase chain aiming to improve the coverage of InSAR deformation map over low-coherence environments. Specific concern is given to the interval phase chain recovery from coherent measurements of PS and DS. The core of the reconstructing interval phase relies on two successive WLS procedures in time and space. The main advantage of the proposed method lies in its robustness despite the coherence estimation bias and the inconsistent noise levels due to different decorrelation mechanisms. The derived unwrapped phase saves extra computation burden for phase unwrapping. In addition, the linear formation makes the implementation flexible for a small subset of interferograms.

We demonstrate the effectiveness of the method from extensive experiments using simulated and real SAR data sets. The simulation experiments show that despite the coherence estimation error, the method can achieve stable estimation. The simulation also shows that using weighted spatial integration according to the *posteriori* phase variance outperforms the state-of-the-art methods in the case with different decorrelation mechanisms. In the real data application over Zhouqu, the reconstructed phases extend the coverage of measurement points compared with PSI processing, facilitating landslide identification and further interpretation.

Appendix

This appendix is dedicated to the description of the determination of the initial weight matrix during arc estimation. As aforementioned, the initial weight matrix $\boldsymbol{P}$ has a diagonal form

$$\boldsymbol{P} = \mathrm{diag}(p^{1,1}, p^{2,2}, \ldots, p^{m,n}, \ldots, p^{N,N}). \tag{17}$$

Because the arc observations represent the phase differences from two connected points, the diagonal element of $\boldsymbol{P}$ can be defined based on the combination of weight factors of two coherent points

$$p_{x,y}^{m,n} = \frac{1}{1/p_x^{m,n} + 1/p_y^{m,n}} \tag{18}$$

where x and y correspond to point indexes. For a single coherent point, the weight factor can be determined by the Fisher information index of interferometric phase [18]

$$p_x^{m,n} = \frac{2L(\gamma_x^{m,n})^2}{1 - (\gamma_x^{m,n})^2} \tag{19}$$

where m and n are the indexes of the SAR image. By combining (18) and (19), the initial matrix for each arc observation can be uniquely determined according to the coherence matrix and multilooking factor of the connected coherent points. We remark that for point-wise PS measurement, because its coherence value is always equal to one [11], the initial weight matrix between two PS measurements can be defined as the diagonal element of an identity matrix

$$\boldsymbol{P}_{x,y}^{\mathrm{PS}} = \boldsymbol{I}_{N(N-1)/2}. \tag{20}$$

Acknowledgment

The authors would like to thank the Japan Aerospace Exploration Agency (JAXA) for providing the ALOS/PALSAR data via Project ER2A2N045 and 3381. They would also like to thank two anonymous reviewers for their constructive suggestions.

References

[1] Z. Lu and D. Dzurisin, *InSAR Imaging of Aleutian Volcanoes: Monitoring a Volcanic Arc From Space* (Geophysical Sciences). Berlin, Germany: Springer-Verlag, 2014.

[2] Y. Fialko, "Evidence of fluid-filled upper crust from observations of postseismic deformation due to the 1992 Mw7.3 Landers earthquake," *J. Geophys. Res., Solid Earth*, vol. 109, no. B8, 2004, Art. no. B08401.

[3] Q. Sun, L. Zhang, X. L. Ding, J. Hu, Z. W. Li, and J. J. Zhu, "Slope deformation prior to Zhouqu, China landslide from InSAR time series analysis," *Remote Sens. Environ.*, vol. 156, pp. 45–57, Jan. 2015.

[4] G. Shi, H. Lin, and P. Ma, "A hybrid method for stability monitoring in low-coherence urban regions using persistent and distributed scatterers," *IEEE J. Sel. Topics Appl. Earth Observ. Remote Sens.*, vol. 11, no. 10, pp. 3811–3821, Oct. 2018.

[5] L. Zhang, Z. Lu, X. Ding, H.-S. Jung, G. Feng, and C.-W. Lee, "Mapping ground surface deformation using temporarily coherent point SAR interferometry: Application to Los Angeles basin," *Remote Sens. Environ.*, vol. 117, pp. 429–439, Feb. 2012.

[6] A. Ferretti, C. Prati, and F. Rocca, "Permanent scatterers in SAR interferometry," *IEEE Trans. Geosci. Remote Sens.*, vol. 39, no. 1, pp. 8–20, Jan. 2001.

[7] B. M. Kampes, *Radar Interferometry: Persistent Scatterer Technique*. Dordrecht, The Netherlands: Springer, 2006.

[8] A. Hooper, H. Zebker, P. Segall, and B. Kampes, "A new method for measuring deformation on volcanoes and other natural terrains using InSAR persistent scatterers," *Geophys. Res. Lett.*, vol. 31, no. 23, Dec. 2004, Art. no. L23611.

[9] R. Lanari, O. Mora, M. Manunta, J. J. Mallorqui, P. Berardino, and E. Sansosti, "A small-baseline approach for investigating deformations on full-resolution differential SAR interferograms," *IEEE Trans. Geosci. Remote Sens.*, vol. 42, no. 7, pp. 1377–1386, Jul. 2004.

[10] P. Berardino, G. Fornaro, R. Lanari, and E. Sansosti, "A new algorithm for surface deformation monitoring based on small baseline differential SAR interferograms," *IEEE Trans. Geosci. Remote Sens.*, vol. 40, no. 11, pp. 2375–2383, Nov. 2002.

[11] A. Ferretti, A. Fumagalli, F. Novali, C. Prati, F. Rocca, and A. Rucci, "A new algorithm for processing interferometric data-stacks: SqueeSAR," *IEEE Trans. Geosci. Remote Sens.*, vol. 49, no. 9, pp. 3460–3470, Sep. 2011.

[12] M. Jiang, X. Ding, R. F. Hanssen, R. Malhotra, and L. Chang, "Fast statistically homogeneous pixel selection for covariance matrix estimation for multitemporal InSAR," *IEEE Trans. Geosci. Remote Sens.*, vol. 53, no. 3, pp. 1213–1224, Mar. 2015.

[13] Y. Wang, X. X. Zhu, and R. Bamler, "Retrieval of phase history parameters from distributed scatterers in urban areas using very high resolution SAR data," *ISPRS J. Photogramm. Remote Sens.*, vol. 73, pp. 89–99, Sep. 2012.

[14] A. M. Guarnieri and S. Tebaldini, "On the exploitation of target statistics for SAR interferometry applications," *IEEE Trans. Geosci. Remote Sens.*, vol. 46, no. 11, pp. 3436–3443, Nov. 2008.

[15] H. Ansari, F. De Zan, and R. Bamler, "Sequential estimator: Toward efficient InSAR time series analysis," *IEEE Trans. Geosci. Remote Sens.*, vol. 55, no. 10, pp. 5637–5652, Oct. 2017.

[16] N. Cao, H. Lee, and H. C. Jung, "A phase-decomposition-based PSInSAR processing method," *IEEE Trans. Geosci. Remote Sens.*, vol. 54, no. 2, pp. 1074–1090, Feb. 2016.

[17] G. Fornaro, S. Verde, D. Reale, and A. Pauciullo, "CAESAR: An approach based on covariance matrix decomposition to improve multibaseline–multitemporal interferometric SAR processing," *IEEE Trans. Geosci. Remote Sens.*, vol. 53, no. 4, pp. 2050–2065, Apr. 2015.

[18] S. Samiei-Esfahany, J. E. Martins, F. van Leijen, and R. F. Hanssen, "Phase estimation for distributed scatterers in InSAR stacks using integer least squares estimation," *IEEE Trans. Geosci. Remote Sens.*, vol. 54, no. 10, pp. 5671–5687, Oct. 2016.

[19] H. Ansari, F. De Zan, and R. Bamler, "Efficient phase estimation for interferogram stacks," *IEEE Trans. Geosci. Remote Sens.*, vol. 56, no. 7, pp. 4109–4125, Jul. 2018.

[20] M. Even and K. Schulz, "InSAR deformation analysis with distributed scatterers: A review complemented by new advances," *Remote Sens.*, vol. 10, no. 5, p. 744, May 2018.

[21] R. Touzi, A. Lopes, J. Bruniquel, and P. W. Vachon, "Coherence estimation for SAR imagery," *IEEE Trans. Geosci. Remote Sens.*, vol. 37, no. 1, pp. 135–149, Jan. 1999.

[22] S. Wu, L. Zhang, X. Ding, and D. Perissin, "Pixel-wise MTInSAR estimator for integration of coherent point selection and unwrapped phase vector recovery," *IEEE Trans. Geosci. Remote Sens.*, vol. 57, no. 5, pp. 2659–2668, Aug. 2019.

[23] L. Zhang, X. Ding, and Z. Lu, "Modeling PSInSAR time series without phase unwrapping," *IEEE Trans. Geosci. Remote Sens.*, vol. 49, no. 1, pp. 547–556, Jan. 2011.

[24] J. H. Friedman, J. L. Bentley, and R. A. Finkel, "An algorithm for finding best matches in logarithmic expected time," *ACM Trans. Math. Softw.*, vol. 3, no. 3, pp. 209–226, Sep. 1977.

[25] M. Costantini, F. Malvarosa, and F. Minati, "A general formulation for redundant integration of finite differences and phase unwrapping on a sparse multidimensional domain," *IEEE Trans. Geosci. Remote Sens.*, vol. 50, no. 3, pp. 758–768, Mar. 2012.

[26] Y. Yang, L. Song, and T. Xu, "Robust estimator for correlated observations based on bifactor equivalent weights," *J. Geodesy*, vol. 76, nos. 6–7, pp. 353–358, Jul. 2002.

[27] P. J. Huber and E. M. Ronchetti, *Robust Statistics* (Wiley Series in Probability and Statistics), 2nd ed. Hoboken, NJ, USA: Wiley, 2009.

[28] R. Andersen, *Modern Methods for Robust Regression* (Quantitative Applications in the Social Sciences). Los Angeles, CA, USA: SAGE Publications, 2008.

[29] P. J. Huber, "Robust estimation of a location parameter," *Ann. Math. Statist.*, vol. 35, no. 1, pp. 73–101, Mar. 1964.

[30] E. Hussain, A. Hooper, T. J. Wright, R. J. Walters, and D. P. S. Bekaert, "Interseismic strain accumulation across the central North Anatolian fault from iteratively unwrapped InSAR measurements," *J. Geophys. Res., Solid Earth*, vol. 121, no. 12, pp. 9000–9019, Dec. 2016.

[31] H. Liang, L. Zhang, X. Ding, Z. Lu, and X. Li, "Toward mitigating stratified tropospheric delays in multitemporal InSAR: A quadtree aided joint model," *IEEE Trans. Geosci. Remote Sens.*, vol. 57, no. 1, pp. 291–303, Jan. 2019.

[32] L. Zhang, X. Ding, Z. Lu, H.-S. Jung, J. Hu, and G. Feng, "A novel multitemporal InSAR model for joint estimation of deformation rates and orbital errors," *IEEE Trans. Geosci. Remote Sens.*, vol. 52, no. 6, pp. 3529–3540, Jun. 2014.

[33] S. S. Esfahany and R. Hanssen, "Feasibility assessment of exploitation of distributed scatterers in InSAR stacks over pasture areas for different SAR satellite missions," *Earth Observ. Geomatics Eng.*, vol. 2, no. 2, pp. 64–73, Dec. 2018.

[34] A. M. Guarnieri and S. Tebaldini, "Hybrid Cramér–Rao bounds for crustal displacement field estimators in SAR interferometry," *IEEE Signal Process. Lett.*, vol. 14, no. 12, pp. 1012–1015, Dec. 2007.

[35] R. Abdelfattah, J. M. Nicolas, F. Tupin, and B. Badredine, "InSAR coherence estimation for temporal analysis and phase unwrapping applications," in *Proc. Scanning Present Resolving Future, IEEE Int. Geosci. Remote Sens. Symp. (IGARSS)*, vol. 5, Jul. 2001, pp. 2292–2294.

[36] M. Jiang, X. Ding, and Z. Li, "Hybrid approach for unbiased coherence estimation for multitemporal InSAR," *IEEE Trans. Geosci. Remote Sens.*, vol. 52, no. 5, pp. 2459–2473, May 2014.

[37] M. Costantini, "A novel phase unwrapping method based on network programming," *IEEE Trans. Geosci. Remote Sens.*, vol. 36, no. 3, pp. 813–821, May 1998.

[38] D. C. Ghiglia and L. A. Romero, "Robust two-dimensional weighted and unweighted phase unwrapping that uses fast transforms and iterative methods," *J. Opt. Soc. Amer. A, Opt. Image Sci.*, vol. 11, no. 1, pp. 107–117, Jan. 1994.

[39] R. Chen, W. Yu, R. Wang, G. Liu, and Y. Shao, "Integrated denoising and unwrapping of InSAR phase based on Markov random fields," *IEEE Trans. Geosci. Remote Sens.*, vol. 51, no. 8, pp. 4473–4485, Aug. 2013.

[40] W. B. Abdallah and R. Abdelfattah, "A joint Markov random field approach for SAR interferogram filtering and unwrapping," *IEEE J. Sel. Topics Appl. Earth Observ. Remote Sens.*, vol. 9, no. 7, pp. 3016–3025, Jul. 2016.

[41] H. Xin, "Slew of landslides unmask hidden geological hazards," *Science*, vol. 330, no. 6005, p. 744, 2010.

[42] Q. Sun, J. Hu, L. Zhang, and X. Ding, "Towards slow-moving landslide monitoring by integrating multi-sensor InSAR time series datasets: The Zhouqu case study, China," *Remote Sens.*, vol. 8, no. 11, p. 908, Nov. 2016.

[43] T. Tadono *et al.*, "Generation of the 30 m-mesh global digital surface model by ALOS prism," *ISPRS-Int. Arch. Photogramm., Remote Sens. Spatial Inf. Sci.*, vol. XLI-B4, pp. 157–162, Jun. 2016.

[44] H. Liang, L. Zhang, Z. Lu, and X. Li, "Nonparametric estimation of DEM error in multitemporal InSAR," *IEEE Trans. Geosci. Remote Sens.*, vol. 57, no. 12, pp. 10004–10014, Dec. 2019.

[45] A. Hooper, P. Segall, and H. Zebker, "Persistent scatterer interferometric synthetic aperture radar for crustal deformation analysis, with application to Volcán Alcedo, Galápagos," *J. Geophys. Res.*, vol. 112, no. B7, 2007, Art. no. B07407.

Hongyu Liang (Graduate Student Member, IEEE) was born in Bazhong, China, in 1991. He received the B.S. degree from Southwest Jiaotong University, Chengdu, China, in 2013, and the M.Sc. degree in geomatics from The Hong Kong Polytechnic University, Hong Kong, in 2014, where he is pursuing the Ph.D. degree with the Department of Land Surveying and Geo-Informatics.

His research interests include estimation theory and advanced processing developments for multitemporal synthetic aperture radar (SAR) interferometry and deformation monitoring.

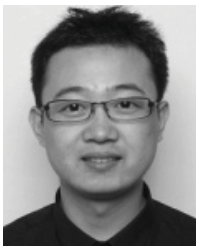

Lei Zhang (Senior Member, IEEE) was born in Yantai, China, in 1981. He received the M.Sc. degree from Tongji University, Shanghai, China, in 2007, and the Ph.D. degree in geodesy and geodynamics from The Hong Kong Polytechnic University, Hong Kong, in 2011. His M.Sc. thesis was on fault slip inversion with interferometric synthetic aperture radar (SAR) and GPS data based on a triangular dislocation model.

Since 2012, he has been a Research Assistant Professor with the Department of Land Surveying and Geo-Informatics, The Hong Kong Polytechnic University. His research interests include developing advanced processing techniques for SAR data and the application of multitemporal interferometric analysis on the retrieval of ground displacement and geophysical parameters, with an emphasis on natural hazard monitoring and mitigation.

Xiaoli Ding (Member, IEEE) received the B.S. degree from the Central South University of Metallurgy (now Central South University), Changsha, China, in 1983, and the Ph.D. degree from The University of Sydney, Sydney, NSW, Australia, in 1993.

He is the Chair Professor of geomatics and the Associate Dean of the Faculty of Construction and Environment, The Hong Kong Polytechnic University, Hong Kong. His research interests include developing technologies for studying ground and structural deformation and geohazards, with a current focus being on spaceborne geodetic technologies such as GPS and interferometric synthetic aperture radar. He has authored more than 300 articles in these research fields.

Prof. Ding is the President of the Sub-Commission 4.4 of the International Association of Geodesy (IAG) on airborne and spaceborne imaging technologies. He is also a fellow of IAG.

Zhong Lu (Senior Member, IEEE) received the B.S. and M.S. degrees from Peking University, Beijing, China, in 1989 and 1992, respectively, and the Ph.D. degree from the University of Alaska Fairbanks, Fairbanks, AK, USA, in 1996.

He was a Physical Scientist with the U.S. Geological Survey (USGS), Vancouver, WA, USA, from 1997 to 2013. He is a Professor and the Endowed Shuler-Foscue Chair with the Huffington Department of Earth Sciences, Southern Methodist University, Dallas, TX, USA. He is also a Principal Investigator of projects funded by NASA, ESA, JAXA, DLR, and USGS on the study of land surface deformation using satellite interferometric synthetic aperture radar (InSAR) imagery. He has authored more than 45 and coauthored 90 peer-reviewed journal articles and book chapters focused on InSAR techniques and applications. His new book is *InSAR Imaging of Aleutian Volcanoes: Monitoring a Volcanic Arc from Space* (Springer, 2014). His research interests include technique developments of SAR, InSAR, and persistent scatterer InSAR processing and their applications on natural hazard monitoring and natural resource characterization.

Dr. Lu is a Committee Member of the International User Team for Radarsat-C SAR Constellations, GeoEarthscope InSAR User Working Group, the NASA's Alaska Satellite Facility User Working Group, and the upcoming NASA-India SAR Science Definition Team. He is also a member of the editorial boards of the *International Journal of Image and Data Fusion*, *Geomatics*, *Natural Hazards and Risk*, and *Dataset Papers in Geosciences*. He was a recipient of the American Society for Photogrammetry and Remote Sensing Award for Best Scientific Paper in *Remote Sensing*, the NASA Group Achievement Award, the NASA Certificate of Appreciation, the Raytheon Distinguished Level Award for Excellence in Technology, Science Applications, the International Corporation Technical Fellow, and the Jerald Cook Memorial Award. He is the Chair of the Western North America InSAR Consortium. He is an Associate Editor of *Remote Sensing* and *Frontier in Volcanology*.

Xin Li was born in Tai'an, Shandong, China, in 1990. She received the B.S. degree in geography information science from the Shandong University of Science and Technology, Qingdao, China, in 2012, and the M.S. degree in geoinformation science from The Chinese University of Hong Kong (CUHK), Hong Kong, in 2013.

She is with the Institute of Geographic Sciences and Natural Resources Research, Chinese Academy of Sciences, Beijing, China. Her research interests include the atmospheric remote sensing application and spatial–temporal analysis.

Jun Hu (Member, IEEE) received the M.Eng. and Ph.D. degrees in geodesy and surveying engineering from Central South University, Changsha, China, in 2008 and 2013, respectively.

From 2013 to 2014, he was a Post-Doctoral Fellow with the Department of Land Surveying and Geo-Informatics, The Hong Kong Polytechnic University, Hong Kong. He is a Full Professor with the Department of Surveying and Remote Sensing, School of Geosciences and Info-Physics, Central South University. He has authored more than 20 articles in international peer-reviewed journals. His research interests include mapping 3-D surface displacement with interferometric satellite synthetic aperture radar technique and its applications in geophysical fields.

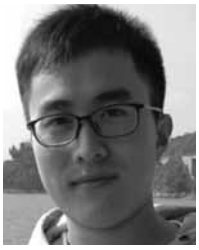

Songbo Wu (Graduate Student Member, IEEE) was born in Xinjiang, China, in 1990. He received the M.Sc. degree from Southwest Jiaotong University, Chengdu, China, in 2015. He is pursuing the Ph.D. degree with the Department of Land Surveying and Geo-Informatics, The Hong Kong Polytechnic University, Hong Kong.

His research interests include advanced processing developments for multitemporal synthetic aperture radar interferometry and the applications on ground deformation continuous monitoring.